



HAL
open science

Investigation of long acoustic waveguides for the very low frequency characterization of monolayer and stratified air-saturated poroelastic materials

Erick Ogam, Zine El Abiddine Fellah, Géry Ogam, Nicholas O Ongwen,
Andrew O Oduor

► To cite this version:

Erick Ogam, Zine El Abiddine Fellah, Géry Ogam, Nicholas O Ongwen, Andrew O Oduor. Investigation of long acoustic waveguides for the very low frequency characterization of monolayer and stratified air-saturated poroelastic materials. *Applied Acoustics*, 2021, 182, pp.108200. 10.1016/j.apacoust.2021.108200 . hal-03250845

HAL Id: hal-03250845

<https://hal.science/hal-03250845>

Submitted on 11 Oct 2021

HAL is a multi-disciplinary open access archive for the deposit and dissemination of scientific research documents, whether they are published or not. The documents may come from teaching and research institutions in France or abroad, or from public or private research centers.

L'archive ouverte pluridisciplinaire **HAL**, est destinée au dépôt et à la diffusion de documents scientifiques de niveau recherche, publiés ou non, émanant des établissements d'enseignement et de recherche français ou étrangers, des laboratoires publics ou privés.

1 Investigation of long acoustic waveguides for the very low
2 frequency characterization of monolayer and stratified
3 air-saturated poroelastic materials

4 Erick Ogam^{a,*}, Zine El Abiddine Fellah^a, Géry Ogam^b, Nicholas O. Ongwen^c, Andrew
5 O. Oduor^c

6 ^a*Laboratoire de Mécanique et d'Acoustique LMA - UMR 7031 AMU - CNRS - Centrale Marseille, 4*
7 *impasse Nikola Tesla CS 40006, 13453 Marseille Cedex 13, France*

8 ^b*Independent Consultant*

9 ^c*Maseno University, Department of Physics and Material Sciences, Maseno, Kenya*

10 **Abstract**

When sound propagates in a porous medium, it is attenuated via several energy loss mechanisms which are switched on or off as the excitation frequency varies. The classical way of measuring acoustic energy loss in porous materials uses the Kundt impedance tube. However, due to its short length, measurements are made in the steady state harmonic regimes. Its lower cutoff frequency is often limited to a few hundreds of Hertz. Two long acoustic waveguides were assembled from water pipes and mounted to create test-rigs for the low-frequency acoustic characterization of monolayer and stratified air-saturated poroelastic materials. The first waveguide was straight and had a length of 120 m, while the second was coiled to gain space and was 135 m long. The long waveguides appeal to very low frequency measurements using impulsive acoustic waves (with rich spectral content) because the incident waves can be separated in time from echoes off the extremities of the guides. The transmission coefficient of porous materials recovered using the two waveguides compared well with those from the transfer matrix method (TMM) used here in combination with Biot's 1962 theory to describe propagation in porous dissipative media. This wave-material interaction model permitted the recovery of the properties of poroelastic materials from transmitted acoustic waves propagating in air. The parameters involved are the Young's moduli, Poisson ratio and microstructural properties such as tortuosity and permeability. Being able to descend to lower frequencies guarantees the correct verification of the magnitude of the measured transmission coefficient which approaches unity towards the static frequency. The coiled and straight

waveguides were found to be equivalent and provided data down to frequencies of the order of ≈ 12 Hz.

11 *Keywords:* Air-saturated poroelastic, Stratified layers, transfer matrix method,
12 Acoustic waveguide, open-cell plastic foams, low-frequency characterization

13 1. Introduction

14 Stratified layers are often natural structures e.g., geological layers, the human skull,
15 bird's wing bones, wood, or plants' leaves. Man made stratified layers like sandwich
16 structured-composites are composed of a lightweight but thick core separating two stiff
17 light skins. The most commonly used core materials are open- and closed-cell structured
18 foams. The whole structure is often light and efficient in resisting bending and buckling
19 loads[1]. These composite structures are mainly used in aerospace applications like in
20 helicopter rotor blades. Sound absorbing packages need not to be stiff and the cores can
21 be made of limp materials such as natural fiber glass or open cell plastic foams.

22 Acoustic wave propagation in layered media is therefore an important topic for many
23 practical applications, namely medicine, passive noise control, applied geophysics, snow
24 layers, to name but a few.

25 The goal of this study was to design and develop very low-frequency test-rigs in the
26 form of a compact, coiled, long and straight acoustic waveguide for the characterization
27 of air-saturated stratified or monolayer porous materials. In order to succeed in this
28 endeavour, a wave-porous stratified media interaction model was also developed.

29 Previous theoretical and experimental studies were developed for the characterization
30 of *closed-cell foams* using a straight pipe waveguide 22 m long [2]. The closed-cell foams
31 were modeled as equivalent elastic stratified material. A coiled 50 m long pipe was re-
32 ported previously for the characterization of porous materials using the *equivalent fluid*
33 *model* [3] in which the porous frame was considered as rigid. However no previous exper-
34 iments have been done using very long waveguides (length ≥ 120 m) and the stratified
35 layers modeled as poroelastic frames saturated with air.

*Principal corresponding author
Email address: ogam@lma.cnrs-mrs.fr (Erick Ogam)

36 The recent development and the simplification of the susceptibility models in the low-
37 frequency regime [4, 5] are some of the motivating factors for the development of a very
38 low-frequency waveguide characterization test rig. The purpose of such an undertaking
39 is to generate real data for the recovery of new low frequency parameters of porous media
40 immersed in air and eventually also test the robustness of inversion algorithms [6]. Work-
41 ing in the low-frequency regime makes it possible to recover experimentally other new
42 transport parameters for air-saturated porous material like the static viscous tortuosity
43 α_0 and the other visco-inertial parameters characterizing the interactions between the
44 fluid and the structure, introduced recently [7, 8].

45 The classical, but still popular, Kundt's impedance tube [9] in which acoustic ab-
46 sorbing materials are characterized using indirect methods [10, 11, 12], does not allow
47 measurements to be done in the very low-frequency regime. This is because of its short
48 length. The lower cutoff frequency of a waveguide is determined by its length. The mode
49 with the lowest cutoff frequency is the fundamental mode of the waveguide. An open
50 ended cylindrical pipe used as a waveguide resonates at an approximate fundamental
51 frequency as function of the length [13, 14]. Therefore, a long waveguide is necessary to
52 get a very low cutoff frequency. The other advantage of the long pipe over the Kundt
53 tube is its ability to accommodate transient or impulsive time signals with rich spectral
54 content that can be separated temporally from the ones reflected from the end of the
55 pipe.

56 For a circular waveguide, the upper cutoff frequency is determined by its cross-section.
57 The propagating part of the acoustic field below this cutoff frequency in the pipe con-
58 sists only of plane waves. The reasons for using a waveguide instead of a free sound field
59 is that the propagation problem dimension becomes one-dimensional (up to the higher
60 cutoff frequency) i.e., sound waves propagate in one direction as plane waves. This im-
61 plies that the waveguide is inherently low-frequency. The existence of loss mechanisms
62 in different frequency regimes (thermal, inertial or viscous [15]) can further reduce this
63 cutoff frequency if they are within the useful measurement bandwidth of the pipe.

64 Since the phenomena occurring involves the skeleton and the fluid, modeling of the sound-
65 structure interaction using a biphasic model is the most appealing. Remember that the
66 equivalent fluid model is just its approximation [3, 16].

67 A stratified theoretical model based on the Biot 1962 theory [17] and the transfer
68 matrix method were developed to model the data from the long waveguides. In Biot's
69 biphasic fluid-structure interaction theory, the acoustic waves propagate both in the
70 skeletal frame and in the saturating fluid of the open-pore porous material. The 1962
71 version has not been as widely used as the 1956 version [18]. In the former version, Biot
72 introduced a parameter $\mathbf{w} = \phi(\mathbf{U} - \mathbf{u})$ representing the flow of the fluid (\mathbf{U}) relative
73 to the solid (\mathbf{u}). In our study, Gassman's equations [19] in poroelasticity relating dry
74 or drained bulk elastic constants to those for fluid-saturated and undrained conditions
75 are integrated. The recent advances and generalizations of theories of dynamic responses
76 of a fluid in a porous medium using the concepts of dynamic viscous permeability and
77 tortuosity [20] as well as the Champoux Allard [21] and Lafarge [22] thermal permeability
78 models have been integrated into the Biot 1962 model [17].

79 The geometry of the problem and the experimental method for acquiring low-frequency
80 acoustic wave transmission data are described in Section (2.1). The theoretical models
81 are detailed in Section (3). The results are given in Section(4). Discussions on the prob-
82 lems and challenges facing the measurement precision in such long waveguides, and those
83 of the theoretical modeling are discussed in Section(5).

84 2. Materials and Methods

85 2.1. The geometry of the acoustic wave transmission problem

86 The approach to solve the acoustic characterization problem of stratified or mono
87 layers composed of air-saturated porous specimens involves designing and assembling the
88 waveguides, equipping them with transducers (loudspeakers) and sensors (microphones)
89 then acquiring long in length, transmitted low frequency acoustic wave data.

90 The transmission of an acoustic wave through an open-cell cellular panel (plate) of
91 infinite extent bordered on both sides by a fluid of semi-infinite extent is first considered.
92 The incident P-wave (p_i) propagating in the fluid impinges on the panel and at the
93 interface wave mode conversion occurs. In the panel, the P-wave breaks into three waves:
94 a solid borne elastic P-wave (P_1), a fluid borne P-wave (P_2) and a shear wave (P_3). At
95 the second interface, the shear wave (SW) is transmitted by conversion into a P-wave

96 ($p_{t_{p \leftarrow SW}}$), the solid borne elastic P-wave is transmitted into the fluid as a P-wave (P_{tp})
 97 (see Figure 1).

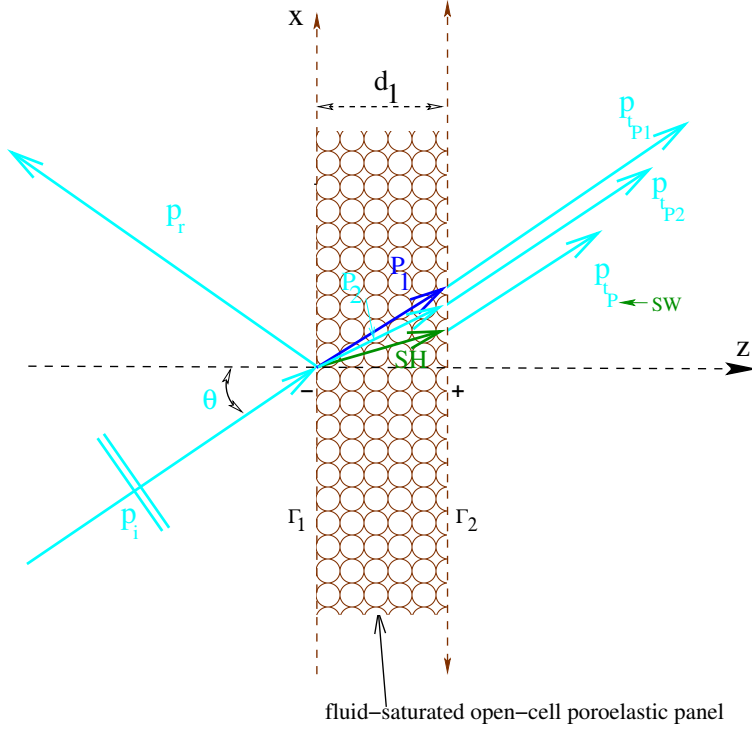


Figure 1: Transmission of acoustic waves by a single layer open-cell panel. The incident compressional wave P_i (Primary (P) wave) travelling in air impinges on the panel. The mode conversions at the host medium - panel interfaces are shown. At the first interface Γ_1 , the P-wave breaks into three waves, a solid borne P-wave (P_1), a fluid borne P-wave (P_2) and a shear wave (SW). At the second interface (Γ_2); the SW is transmitted into the host medium by conversion into a P-wave ($p_{t_{p \leftarrow SW}}$); the solid borne P_1 -wave is transmitted into the fluid as a P-wave ($P_{t_{P_1}}$). The angle of incidence in this study is normal to the specimen.

98 *2.2. The low-frequency acoustic waveguides*

99 The first long waveguide, coiled and therefore more compact, was installed in a nor-
 100 mal room (it could also be moved into an anechoic chamber if necessary). The second
 101 waveguide was kept straight and placed outside the main building hanging under the ceil-
 102 ing of a long parking lot in an exterior climatic and noisy traffic environment (presence
 103 of a moderately busy road nearby).

104 The low and high cutoff frequencies of a waveguide of cylindrical crosssection are
 105 given by

$$f_{LC} = \frac{c_f}{(L + 1.6 a)}, \quad f_{HC} = \frac{1.8412 c_f}{(2\pi a)}, \quad (1)$$

106 where c_f is the sound velocity in the fluid, L is the length of the pipe and a , its radius).

107 2.2.1. The coiled PE pipe waveguide

108 The first acoustic waveguide was composed of segments of 10, 25 and two 50 m
 109 long polyethylene (PE) water pipes (interior diameter 2.54 cm) joined together using
 110 compression nut type mechanical coupling for joining PE pipe to PE pipe. The pipe
 111 waveguide system (total length 135 m) was coiled (average coiled radius: 30 cm) so as
 112 to gain space and be able to fit it into the experimental room (Fig. (2a)). An acoustic
 113 loudspeaker was introduced at one end of the waveguide. It was then driven to generate
 114 an acoustic pulse forcing the pressure to vary in the direction of propagation.

115 2.2.2. The straight PVC pipe waveguide

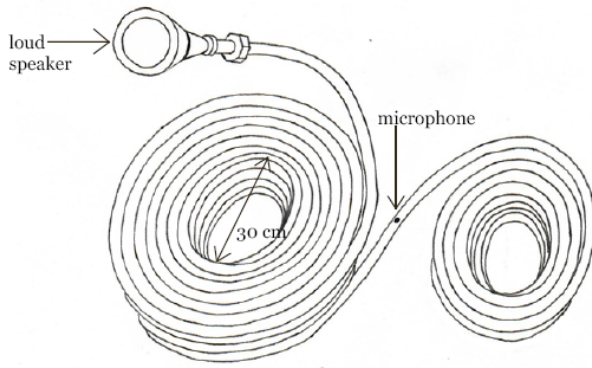
116 The second waveguide was a straight 120 m polyvinyl chloride (PVC) pipe with
 117 internal diameter 34.0mm, external diameter 40.0mm respectively (Fig. 2b and c). It
 118 was composed of 20 polyurethane water pipes (much longer than in Reference [2]) joined
 119 together using fittings and sealed using PVC cement to make the joints air-tight. The
 120 pipe was left straight. Being longer than any available space in the experimental rooms,
 121 it was installed under the ceiling of the roof of the car park shelter of the new site of the
 122 LMA in the north of Marseille.

123 A small microphone was placed midway along the length of the waveguide in order
 124 to capture the acoustic pulse transmitted by the poroelastic layers. The experimental
 125 setup is shown in Fig. (2d).

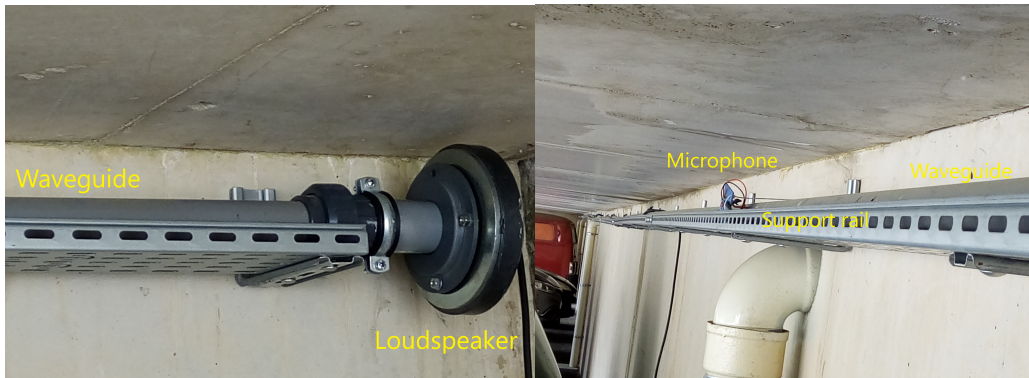
126 The cutoff frequencies are resumed in Table (1)

Waveguide	Diameter (mm)	Length (m)	Lower cutoff (Hz)	Higher cutoff (kHz)
Coiled	25.4	135	2.5	7.9
Straight	34.0	120	2.8	5.9

Table 1: The cutoff frequencies of the two waveguides.

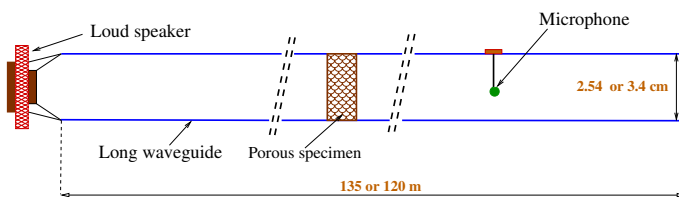


(a)



(b)

(c)



(d)

Figure 2: Sketches and photographs of the low-frequency acoustic waveguide experimental test-rigs. (a) The sketch of the coiled PE pipe waveguide with the loud speaker. (b) The photograph of the setup under the parking lot ceiling with the loud speaker. (c) The straight waveguide downstream. (d) Sketch of the experimental test-rig for the low-frequency measurement of the transmitted acoustic waves.

127 *2.2.3. Capturing the transmitted pressure*

128 The same transducer (exciter) and sensors were used in the coiled and straight wave-
129 guide measurements. A transient wave was generated in the waveguide by a loudspeaker
130 (B&C-DE-700-8, Italy) driven by a waveform function generator (Agilent 33250B, Love-
131 land Colorado, USA) through a power amplifier (B&K2706,). The excitation signal was
132 a Heaviside step function defined as

$$\forall \mathbf{t} \in \mathbb{R}, \mathbf{H}(\mathbf{t}) = \begin{cases} 0, & t < 0, \\ 1, & t \geq 0, \end{cases}$$

133 The step function was produced by synthesizing a long positive rectangular pulse
134 using the function generator. The steep rise in the voltage of the leading edge of the
135 pulse caused the loudspeaker membrane to deform. This induced a very short acoustic
136 pulse wave in the waveguide. An electret condenser omnidirectional microphone sensor
137 with integrated preamplifier (ABM-716-RC Pro-Signal, Omnidirectional, bandwidth 50
138 Hz to 16 kHz, external diameter 3 mm, external height 6 mm) placed downstream of the
139 waveguide captured the transmitted acoustic wave. This response was digitized using
140 a flexible-resolution digitizer (NI-PXI-5922, National Instruments, Austin, TX USA)
141 inserted into a Chassis (NI-PXI-1033) connected to a personal laptop computer running
142 the NIScope data acquisition program.

143 The transmission coefficient (TC) was obtained through the computation of the trans-
144 fer function between the incident pressure obtained in the absence of the specimen and
145 the transmitted pressure in the presence of the specimen. The transfer function $T_{IT}(f)$
146 was computed from the quotient of the cross power spectral density (S_{IT}) of the incident
147 $p_I(t)$ and transmitted acoustic pressure $p_T(t)$ and the power spectral density (S_{II}) of
148 $p_I(t)$.

$$T_{IT}(f) = \frac{S_{IT}(f)}{S_{II}(f)}.$$

149 which were computed using the programming languages: Matlab® and the free Julia
150 programming language [23]). In this study an example computer code is given in Ap-
151 pendix A).

152 **3. The transfer matrix method**

153 In this study the transfer matrix method (TMM) was developed to analyze the propa-
 154 gation of acoustic waves in the stratified porous layers. Computations and measurements
 155 were first undertaken for fluid-saturated monolayer open-cell foams and then for fluid sat-
 156 urated stratified layers. The TMM model was based on the Biot 1962 theory [24]. The
 157 alternative description by Johnson et al [20] of the viscous frictions inside the boundary
 158 layers in the vicinity of the solid walls was employed. It gives more physical insight
 159 into these interactions. The thermal effects model, developed by Champoux, Allard [25]
 160 and Lafarge [22] was also employed. These improvements added to the Biot model are
 161 highlighted in Appendix B. The complete model is abbreviated herein, BJKCAL.

162 The equations of motion were derived from constitutive equations relating stresses
 163 and pressure to the strains and fluid flow [24] (using indicial notation, ιj)

$$\begin{aligned}\tau_{\iota j} &= 2\mu \varepsilon_{\iota j} + \delta_{\iota j} ((H - 2\mu)\varepsilon - C\xi), \\ p_f &= -C\varepsilon + M\xi,\end{aligned}\tag{2}$$

164 where μ is the shear modulus, $H = \lambda_c + 2\mu$, $\lambda_c = \lambda + \alpha_B^2 M$ (λ is Lamé's coefficient),
 165 $C = \alpha_B M$, $M = \frac{K_f/\phi}{1 + D}$ is the complex modulus, $D = (\alpha_B - \phi) \frac{K_m/\phi}{K_s}$, the Biot-
 166 Willis [26] constant $\alpha_B = 1 - K_m/K_s$, K_s is the bulk modulus of the solid matrix, K_m
 167 is the drained (dry) bulk modulus and K_f is the bulk modulus of the pore fluid, ε_{kl} are
 168 the components of the infinitesimal strain tensor and $\delta_{\iota j}$ is the Kronecker delta function:

$$\delta_{\iota j} = \begin{cases} 1, & \iota = j, \\ 0, & \iota \neq j. \end{cases}$$

169 The relative density $\zeta = (\rho_m/\rho_s)$ (ρ_s is the density of the solid matrix and ρ_m is the
 170 density of the drained skeleton). The Young's modulus of the dry skeletal frame is given
 171 by:

$$E_m = C_1 E_s (1 - \phi)^2, \quad \phi = 1 - \zeta,\tag{3}$$

172 where E_s is Young's modulus of the solid matrix and ϕ is the porosity. For open-cell PU
 173 foam $C_1 \approx 1$ [27].

174 From the constitutive equations are derived the two motion equations expressing the
 175 dynamic inertial motion of the whole fluid-solid system in terms of the stresses. They

176 are written (using vector calculus notation):

$$\begin{aligned}\nabla \cdot \boldsymbol{\tau} &= \mu \nabla^2 \mathbf{u} + \nabla [(H - \mu)\boldsymbol{\varepsilon} - C\boldsymbol{\xi}] = \frac{\partial^2}{\partial t^2}(\rho \mathbf{u} + \rho_f \mathbf{w}), \\ \nabla(C\boldsymbol{\varepsilon} - M\boldsymbol{\xi}) &= \rho_f \frac{\partial^2}{\partial t^2} \mathbf{u} + \varrho(t) * \frac{\partial^2}{\partial t^2} \mathbf{w},\end{aligned}\quad (4)$$

177 where ρ is the density of the mixture (composite), ρ_f is that of the fluid, \mathbf{u} and \mathbf{U} are the
 178 solid and fluid displacements, respectively. The fluid displacement relative to the frame,
 179 $\mathbf{w} = \phi(\mathbf{U} - \mathbf{u})$ and ϕ is the porosity. The increase in fluid content $\boldsymbol{\xi} = -\nabla \cdot \mathbf{w}$ and the
 180 volumetric strain of the solid $\boldsymbol{\varepsilon} = \nabla \cdot \mathbf{u}$. The equivalent density in the time domain is $\varrho(t)$
 181 and can also be represented as $\tilde{\varrho}(\omega) = \rho_f \alpha(\omega) / \phi$ in the frequency domain.

182 The derivation of the wavenumbers and phase velocities are given in Appendix C.

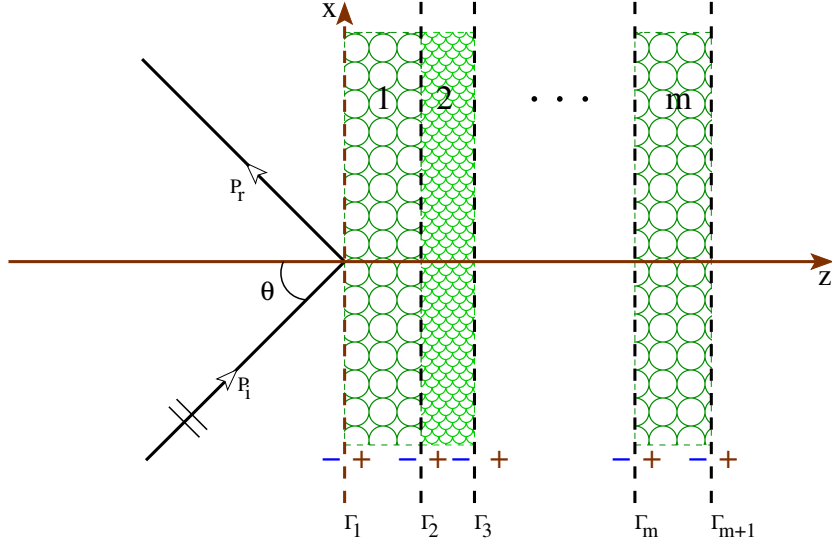


Figure 3: The sketch of the stratified fluid saturated poroelastic layers.

183 In order to model wave propagation in a poroelastic layer (Fig. 3), the acoustic wave
 184 field in the layer is characterized by the wave speeds and the stresses in the fluid and
 185 solid phases. In this context two state vectors $\mathbf{V}(M_{\Gamma_m^+})$ and $\mathbf{V}(M_{\Gamma_{m+1}^+})$ at the first and
 186 second points $M_{\Gamma_m^+}$ and $M_{\Gamma_{m+1}^-}$ on the interfaces at Γ_m^+ and Γ_{m+1}^- of a fluid saturated

187 poroelastic layer m are chosen as:

$$\begin{aligned}
 \mathbf{V}(M_{\Gamma_m^+}) &= \left[\dot{u}_x^s(M_{\Gamma_m^+}) \quad \dot{u}_z^s(M_{\Gamma_m^+}) \quad \dot{u}_z^f(M_{\Gamma_m^+}) \quad \tau_{zz}^s(M_{\Gamma_m^+}) \quad \tau_{xz}^s(M_{\Gamma_m^+}) \quad \tau_{zz}^f(M_{\Gamma_m^+}) \right]^T \\
 \mathbf{V}(M_{\Gamma_{m+1}^-}) &= \left[\dot{u}_x^s(M_{\Gamma_{m+1}^-}) \quad \dot{u}_z^s(M_{\Gamma_{m+1}^-}) \quad \dot{u}_z^f(M_{\Gamma_{m+1}^-}) \quad \tau_{zz}^s(M_{\Gamma_{m+1}^-}) \quad \tau_{xz}^s(M_{\Gamma_{m+1}^-}) \quad \tau_{zz}^f(M_{\Gamma_{m+1}^-}) \right]^T,
 \end{aligned} \tag{5}$$

188 where the "overdot" represents the derivative with respect to time. The state vectors
 189 can be rewritten in matrix form as:

$$\begin{aligned}
 \mathbf{V}(M_{\Gamma_m^+}) &= [\mathbf{T}_m(M_{\Gamma_m^+})]\mathbf{A} \\
 \mathbf{V}(M_{\Gamma_{m+1}^-}) &= [\mathbf{T}_m(M_{\Gamma_{m+1}^-})]\mathbf{A},
 \end{aligned} \tag{6}$$

190 where $[\mathbf{T}_m]$ is the transmission matrix of the stresses and velocities and \mathbf{A} a vector to be
 191 determined.

192 The derivation of the matrix formulation is given in Appendix D

193 The derived matrix equation for air saturated stratified bilayer poroelastic plates
 194 insonified by a plane wave at an oblique angle of incidence θ_i is therefore given in Eq. (7):

$$\begin{bmatrix}
(1-\phi_I)T_{21}^g + \phi_I T_{31}^g & (1-\phi_I)T_{22}^g + \phi_I T_{32}^g & (1-\phi_I)T_{23}^g + \phi_I T_{33}^g & (1-\phi_I)T_{24}^g + \phi_I T_{34}^g & (1-\phi_I)T_{25}^g + \phi_I T_{35}^g & (1-\phi_I)T_{26}^g + \phi_I T_{36}^g & \frac{p_i \cos(\theta_i)}{z_A} & 0 & 0 \\
T_{41}^g & T_{42}^g & T_{43}^g & T_{44}^g & T_{45}^g & T_{46}^g & (1-\phi_I)p_i \cos(\theta_i) & 0 & 0 \\
T_{51}^g & T_{52}^g & T_{53}^g & T_{54}^g & T_{55}^g & T_{56}^g & 0 & 0 & 0 \\
T_{61}^g & T_{62}^g & T_{63}^g & T_{64}^g & T_{65}^g & T_{66}^g & \phi_I p_i \cos(\theta_i) & 0 & 0 \\
0 & 1-\phi_m & \phi_m & 0 & 0 & 0 & 0 & -\frac{p_i \cos(\theta_i)}{z_B} & 0 \\
0 & 0 & 0 & 1 & 0 & 0 & 0 & (1-\phi_m)p_i \cos(\theta_i) & 0 \\
0 & 0 & 0 & 0 & 1 & 0 & 0 & 0 & 0 \\
0 & 0 & 0 & 0 & 0 & 1 & 0 & 0 & 0 \\
\hline
\hat{u}_x^s(\mathbf{\Gamma}_{m+1}^-) & \hat{u}_y^s(\mathbf{\Gamma}_{m+1}^-) & \hat{u}_z^s(\mathbf{\Gamma}_{m+1}^-) & \tau_{zz}^s(\mathbf{\Gamma}_{m+1}^-) & \tau_{xz}^s(\mathbf{\Gamma}_{m+1}^-) & \tau_{zx}^s(\mathbf{\Gamma}_{m+1}^-) & R & T & \\
\hline
\frac{p_i \cos(\theta_i)}{z_A} & -(1-\phi_I)p_i \cos(\theta_i) & 0 & -\phi_I p_i \cos(\theta_i) & 0 & 0 & 0 & 0 & 0
\end{bmatrix} = \begin{bmatrix}
\frac{p_i \cos(\theta_i)}{z_A} & 0 & 0 & 0 & 0 & 0 & 0 & 0 & 0 \\
-(1-\phi_I)p_i \cos(\theta_i) & 0 & 0 & 0 & 0 & 0 & 0 & 0 & 0 \\
0 & -\phi_I p_i \cos(\theta_i) & 0 & 0 & 0 & 0 & 0 & 0 & 0 \\
-\phi_I p_i \cos(\theta_i) & 0 & 0 & 0 & 0 & 0 & 0 & 0 & 0 \\
-\frac{p_i \cos(\theta_i)}{z_B} & (1-\phi_m)p_i \cos(\theta_i) & 0 & 0 & 0 & 0 & 0 & 0 & 0 \\
(1-\phi_m)p_i \cos(\theta_i) & 0 & 0 & 0 & 0 & 0 & 0 & 0 & 0 \\
0 & 0 & 0 & 0 & 0 & 0 & 0 & 0 & 0 \\
0 & 0 & 0 & 0 & 0 & 0 & 0 & 0 & 0 \\
0 & 0 & 0 & 0 & 0 & 0 & 0 & 0 & 0
\end{bmatrix} \times \quad (7)$$

196 **4. Results**

197 *4.1. The poroelastic material samples*

198 The air saturated porous foam materials used for this study were open-cell yellow and
 199 gray polyurethane (PU) and melamine foam panels. Their micro-visco-acoustic param-
 200 eters are given in Table (2). The mechanical parameters (Biot Willis parameters [26]) are
 201 given Table (3). These parameters were from our previously reported results, but, some
 202 parameters like Poisson ratio were fine-tuned a little bit to match the experimental data.

Specimen	ϕ	Λ ($\times 10^{-6}$ m)	$\frac{\Lambda'}{\Lambda}$	σ (Pa.m ⁻² .s)	α_∞	k'_0 ($\times 10^{-9}$ m ²)
Yellow PU Foam	0.98	120	2.8	5200	1.2	5.0
Gray PU Foam	0.98	120	2.0	5000	1.15	3.5
Melamine Foam	0.99	100	2.0	10000	1.01	8.0

Table 2: Values of the parameters recovered using real data and solving an inverse problem [28, 29] for the three open-cell foam specimens.

203

Specimen	ρ (kg/m ³)	ρ_s (kg/m ³)	E_s (Gpa)	E_m (Pa)	ν_m
Yellow PU Foam	24	1200	0.48	190×10^3	0.45
Gray PU Foam	28	1400	0.48	185×10^3	0.40
melamine Foam	8.35	1570	7.4	180×10^3	0.47

Table 3: Mechanical parameters for the open-cell plastic porous foam specimens [15].

204 *4.2. Validation of the experimental setup and the prediction model*

205 The incident pressure (captured in the absence of the specimen) and the transmitted
 206 pressure (with the specimen) and their corresponding power spectral densities for a 1.0
 207 cm thick open-cell porous gray polyurethane foam (GPUF) in the 135 m long coiled
 208 waveguide, are depicted in Fig. (4)a and b respectively. The comparison between the
 209 experimental and theoretical transmission coefficients are also shown (Fig. (4)c). This
 210 can be considered as a thin specimen, it has a high transmission coefficient off the static
 211 frequency. The lowest cutoff frequency in this case is ≈ 12 Hz and $|T| \rightarrow 1$. The higher

212 cutoff frequency (≈ 1200 Hz) is lower than the theoretical one of 7.9 kHz. The limit
 213 manifests itself by the presence of oscillations (i.e., noise) in the transmission coefficient.
 214 A close examination shows that the deviation from the theoretical model starts at about
 500 Hz. This is explained later in the discussion section 5.2.

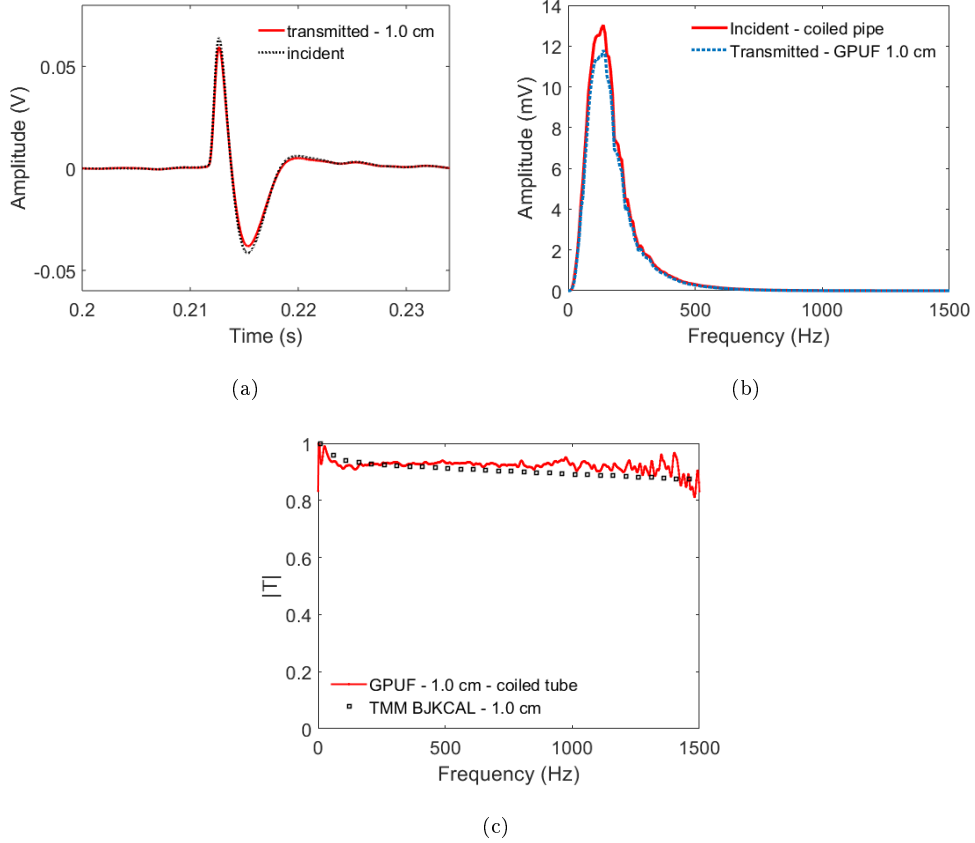


Figure 4: The transmission coefficient for a single porous layer inserted into the coiled waveguide, (a) The incident and transmitted temporal signals. (b) Their power spectral densities. (c) The computed TMM BJKCAL model (squares) and the experimental (solid line) transmission coefficients for an open-cell GPUF (1.0 cm thick).

215

216 4.3. Comparing the measurement performance of the two pipes using a monolayer of an 217 air-saturated poroelastic material

218 Two monolayer foams of the same material and the same thickness (but with dif-
 219 ferent diameters, 2.54 cm and 3.4 cm) were characterized in the coiled and the straight

220 waveguides. The transmission coefficient data obtained from the two waveguides using
 221 the same foam material were compared against the theoretical model. The two single
 222 layer foams were machined from a 1.0 cm thick yellow polyurethane foam (YPUF). The
 223 comparison between the three transmission coefficients obtained for each of the speci-
 224 mens with those from the corresponding theoretical model data computed for the foam
 225 are shown in Fig. (5)a and b. This demonstrates that the straight and coiled waveguides
 226 are equivalent and that the bends of the coiled pipe do not affect the measurements
 227 in the useful bandwidth considered (from the lower cutoff frequency, ≈ 12 Hz, up to
 228 the frequencies where the oscillations start indicating that the signal to noise ratios are
 229 lower, i.e., ≈ 1100 Hz for the straight pipe and ≈ 800 Hz for the straight one). There
 230 is more noise in Fig. (5)a than Fig. (5)b because the coiled pipe is longer in length
 231 (longer air column), therefore the acoustic wave is more attenuated resulting in a lower
 232 signal to noise ratio. The change from the viscous energy loss mechanism regime to the
 233 inertial loss regime [15] at ≈ 500 Hz is the reason for the sudden increase in attenuation
 234 as frequency increases. This is discussed in detail later in section 5.2.

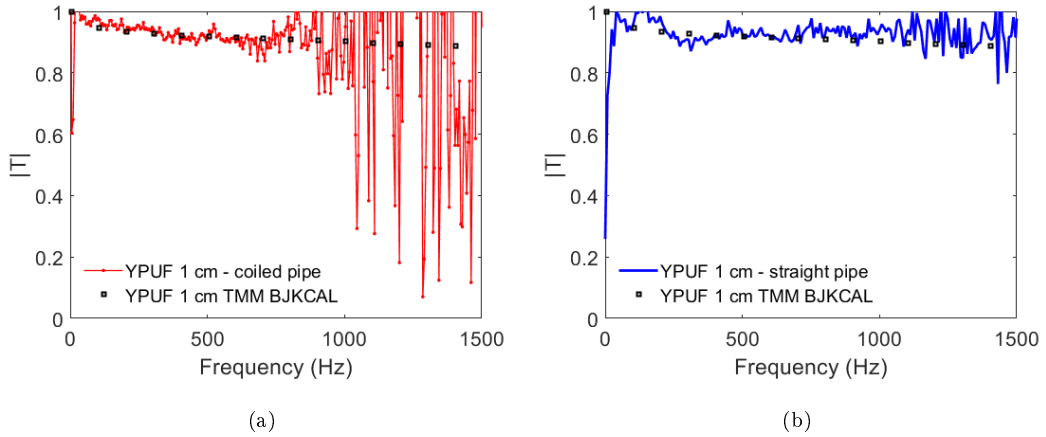
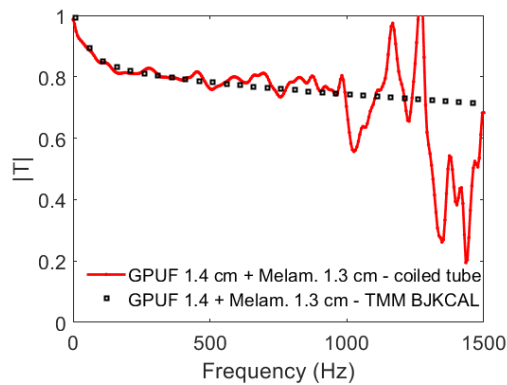


Figure 5: The transmission coefficients for two single layers of YPUF (1.0 cm thick), of diameters 2.54 cm and 3.4 cm inserted in the coiled and straight waveguides respectively. Comparison between the computed TMM BJKCAL model transmission coefficient and the experimental ones obtained from each waveguide, (a) TC in the coiled waveguide, (b) the straight waveguide.

235 *4.4. Measurement performance of the coiled pipe using a stratified layer of an air-saturated*
 236 *poroelastic material*

237 This configuration involves a 1.4 cm thick GPUF foam and a 1.3 thick melamine foam,
 238 in simple contact to form a stratified layer. In this configuration, the TC measured in
 239 the coiled pipe (Figure (6)) off and near the static frequency agrees well with that of the
 TMM BJKCAL model.



(a)

Figure 6: Comparisons between the theoretical (TMM BJKCAL) and the measured TCs of stratified (double) layers composed of a 1.4 cm and 1.3 cm thick GPUF and melamine foams respectively.

240

241 **5. Discussion**

242 *5.1. Improvement of the TC measurements near the static frequency - use of thick sam-*
 243 *ples meticulously slid into the waveguide for proper boundary conditions*

244 It has previously been reported that the adverse effect on the results due to shearing
 245 vibration resonance can be mitigated by the cutting accuracy (radius and circularity) of
 246 the materials [30]. Some studies have proposed placing rings on each material surface [31].

247

248 In order to put into light the problems that degrade the precision of the measurements,
 249 thin samples of melamine and yellow polyurethane foam, both of thickness 1.0 cm, were
 250 tested. The TCs are shown in Fig. (7). In this configuration, the assumed boundary
 251 conditions between the two foams gives an acceptable prediction of the transmission

252 coefficient off the static frequency (i.e., frequency > 100 Hz). The mismatches with the
 253 theoretical model near the static frequency are of the same type for the two waveguides.
 254 It is important to note that the lower cutoff frequency of the microphone is 50 Hz,
 255 implying that reducing the amplitude will only result in a poor signal to noise ratio near
 256 the static frequency.

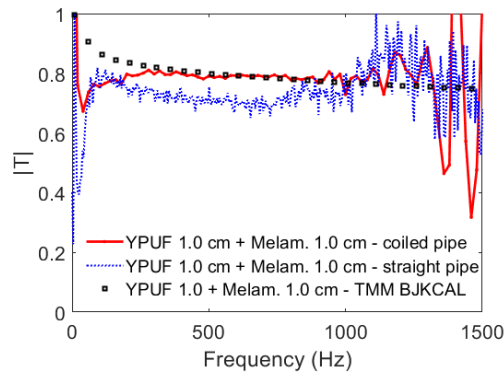


Figure 7: Comparisons between the theoretical (TMM BJKCAL) and experimental TCs of stratified (double) layers composed of a YPUF (1.0 cm thick) and melamine (1.0 cm thick) in simple contact placed in the coiled and straight pipes.

257 The other reason for the TCs of thinner lighter foam samples being poorly captured
 258 near the static frequency is that, at the lower frequencies, the samples are displaced
 259 mechanically (blown aside) at the passage of the low frequency acoustic impulsive wave.
 260 The force of the transient burst displaces the thin low density samples. This makes the
 261 air tightness of the boundary conditions between the specimen and the pipe difficult to
 262 achieve. One of the remedies is to reduce the amplitude of the acoustic pulse in the pipe,
 263 but without compromising the signal to noise ratio especially in the frequency regimes
 264 where the attenuation mechanisms come into play.

265 The transmission coefficients of thick monolayer samples of GPUF and melamine foam
 266 both (2.5 cm thick) were obtained and found to match the theory well (Fig. 8). These
 267 results confirm that the mismatch between theory and experiments at low frequencies
 268 can therefore mainly be explained by the lightweight nature of the thin melamine foam
 269 samples (easily displaced by the impulsive wave) and the lower cutoff frequency of the
 270 microphone.

271 A closer and systematic study on how to improve the measurement of the TC for
 272 thinner samples and the confection of a non invasive sample holder will be undertaken.
 273 Such a task will be easier to accomplish since the TMM BJKCAL model, developed
 274 herein, has proved to be accurate and robust to model the experiment.

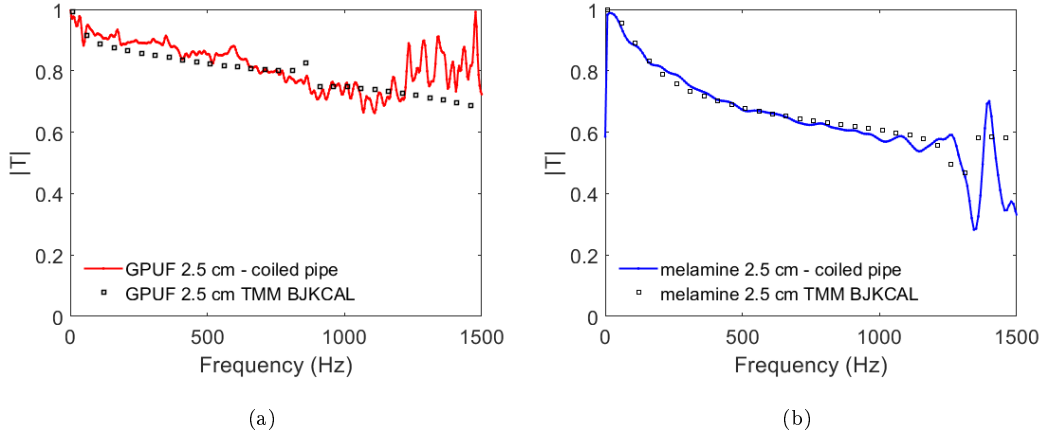


Figure 8: Comparison between (a) The experimental TC of a single layer GPUF (2.5 cm thick), (b) that of a single layer melamine foam (2.5 cm thick), with the theoretical TC data computed using the TMM BJKCAL model. The measurements were done in the coiled waveguide (135 m long).

275 5.2. The measurement bandwidth of the waveguides

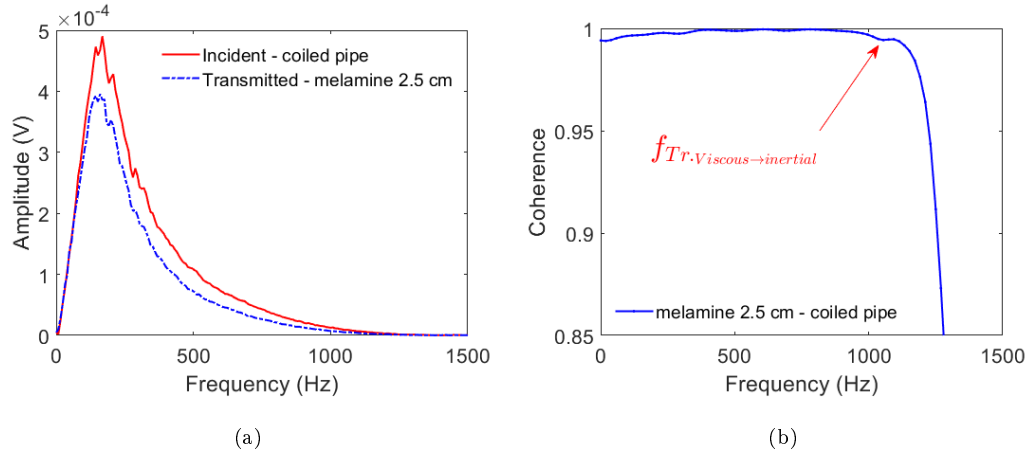
276 The upper theoretical cutoff frequency of the straight waveguide (diameter 34 mm)
 277 is $f_{HC} \approx 5.9\text{kHz}$ and that of the coiled pipe (diameter 25.4 mm) is $\approx 7.9\text{kHz}$ (using
 278 expressions in Eqn. 1, see Table 1). In reality, these cutoff frequencies of the waveguides
 279 containing the specimens are lower. A close examination of the transmission coefficients
 280 indicate that this is due to the lower signal to noise ratio as a result of the energy loss
 281 mechanisms in porous material in the long waveguides.

282 In this study the coherence function [32, 33] was employed to estimate the causality
 283 between the incident and transmitted pressure signals in order to determine the frequency
 284 where the signal to noise ratio becomes too low. The magnitude coherence estimate is a
 285 function of frequency with values between 0 and 1. It indicates how well the two signals
 286 correspond to each other at each frequency (i.e, estimates the causality between the input

and output) is:

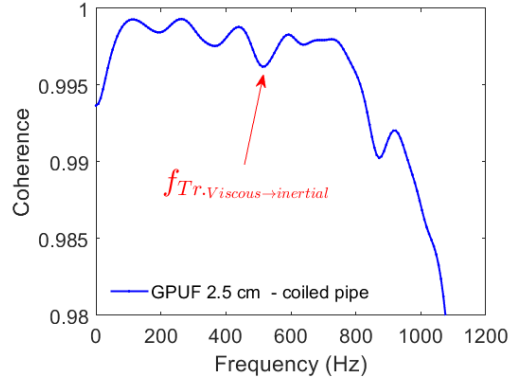
$$C_{IT}(\omega) = \frac{|S_{IT}(\omega)|^2}{S_{II}(\omega)S_{TT}(\omega)}. \quad (8)$$

It is therefore the best tool to determine the useful bandwidth of the waveguides. This bandwidth depends on the attenuation of the porous specimens in the pipes and somehow on the length of the air column.



(a)

(b)



(c)

Figure 9: (a) The spectrum of the incident (without the foam) and transmitted pressure signals for the single layer melamine (2.5 cm thick) foam in Fig. 8b. The coherence between their incident and transmitted acoustic pressure signals (b) the melamine foam, (c) the GPUF foam. The measurements were done in the coiled waveguide (135 m long).

Coherence is consequently used to visualize the bandwidth of the system. The spectrum of the two signals captured for the single layer of melamine foam (2.5 cm thick) and

293 its coherence magnitude are plotted in Fig. (9)a and b. The coherence for a GPUF (2.5
 294 cm thick) is depicted in Fig. (9)c. The upper cutoff frequencies for the melamine and
 295 GPUF are ≈ 1200 Hz and 520 Hz respectively. Coincidentally these are the acoustic loss
 296 mechanism transition frequencies where the acoustic energy loss mechanism transitions
 297 from the viscosity dominated one to the inertia dominated regime [15]. This frequency
 298 is given by

$$f_{Tr.viscous \rightarrow inertial} = \frac{\sigma \phi}{2\pi \rho_f \alpha_\infty}.$$

299 Employing values from Table (2) and the above expression, $f_{Tr.viscous \rightarrow inertial} = 1200$
 300 Hz and 525 Hz for the melamine foam and the GPUF respectively.

301 Although the theoretical lower cutoff frequency for the long waveguide is $f_{LC} \approx 2.5$
 302 Hz, the dip of the coherence near the static frequency is due to the cutoff frequency of
 303 the microphone. This is situated around 50 Hz (the microphone manufacturer) but the
 304 coherence is acceptable up to $f_{LC} \approx 12$ Hz. This implies that a microphone with a lower
 305 cutoff frequency can improve the coherence in this frequency zone.

306 6. Conclusion

307 The two test-rigs composed of long pipe waveguides, one straight and the second
308 coiled, were found to appeal to the low-frequency characterization of porous open-cell
309 materials. The transmission coefficient data obtained from the two waveguides for mono-
310 layer and stratified layers of air-saturated poroelastic materials were found to agree with
311 those obtained from the transfer matrix method that employs the 1962 version of the
312 Biot interaction model [24] (the model takes into account the fluid and skeletal interac-
313 tion). The advantage of the low frequency measurement is, it allows the verification of
314 the value of the transmission coefficient. It is unity at the static frequency. The favor-
315 able agreement between the measured transmission coefficients in the waveguides with
316 the prediction model make these devices appealing to the recovery of Young's modu-
317 lus, Poisson ratio of the skeletons and the micro-geometrical properties such as porosity,
318 tortuosity of sound absorbing air-saturated poroelastic materials in air.

319 The lowering of the bandwidth of the waveguides through the frequency dependent
320 loss mechanisms in the layers and the cutoff frequency of the acoustic sensor were observed
321 using the coherence function. These factors resulted in a loss of coherence between the
322 incident and transmitted waves for the lower cutoff at around 50 Hz and the higher
323 cutoff at ≈ 1100 Hz for the melamine foam and ≈ 500 Hz for the GPF. Meaning
324 that the upper cutoff frequency was way below the theoretical cutoff (higher) frequencies
325 of the waveguides. These cutoff frequencies were found to correspond to the transition
326 frequencies of the air-saturated poroelastic foams, i.e., the passage from the viscous losses
327 regime to the inertial losses regime.

328 It was also established that the coiled and straight pipes gave quasi-identical results
329 in the measurement bandwidth considered. The advantage of the coiled pipe is that it
330 occupies smaller space than the straight one. This is an advantage when the experimental
331 arena space is small. However, the larger cross-section area of the straight pipe provides
332 a better representation of the samples (averaging the material properties over a larger
333 surface area). The wider cross-section means that there is lesser attenuation due to
334 the presence of the rigid walls. An improvement in the precision of determining the
335 transmission coefficient was observed when thicker samples were employed.

336 **Appendix A. Computer coding of the transmission coefficient**

337 Having acquired the incident pressure signal obtained in the absence of the specimen,
 338 p_i , and the transmitted pressure in the presence of the specimen, p_t , the transmission
 339 coefficient can be computed as follows:

```

340 N = length(Pi); % Length of the incident signal
341 xdft = fft(Pi); % compute the fast Fourier transform
342 xdft = xdft(1:N/2+1);
343 psdx = (1/(Fs*N)) * abs(xdft).^2; % compute the psd
344 psdx(2:end-1) = 2*psdx(2:end-1); % conserve the total power X2
345 freq = 0:Fs/N:Fs/2; % form fft frequency
346 ydft = fft(Pt); % compute the fast Fourier transform
347 ydft = ydft(1:N/2+1);
348 psdy = (1/(Fs*N)) * abs(ydft).^2; % compute the psd
349 psdy(2:end-1) = 2*psdy(2:end-1); % conserve the total power X2
350 Sii=xdft.*conj(xdft)/N^2; % auto psd - con -> conjugate
351 Sit=ydft.*conj(xdft)/N^2; % cross psd
352 Tit=abs(Sit./Sii); % compute the transmission coefficient

```

353 **Appendix B. The changes made to improve the frequency behavior of the**
 354 **Biot model**

355 In the frequency domain, two factors, the dynamic tortuosity ($\tilde{\alpha}(\omega)$) and the dynamic
 356 compressibility ($\beta(\omega)$) are modified through multiplication with the fluid densities (ρ_f)
 357 and compressibility (K_f), to obtain the modified parameters of the porous medium ($\rho_e =$
 358 $\rho_f \alpha(\omega)$ and $K_e = K_f \beta(\omega)^{-1}$). These two factors represent the deviation from the non
 359 dissipative behavior of the fluid in free space as the frequency increases.

$$\tilde{\alpha}(\omega) = \alpha_\infty \left(1 + \frac{1}{i\varpi} \sqrt{1 + \frac{M}{2} i\varpi} \right), \quad \varpi = \frac{\omega \alpha_\infty \rho_f}{\sigma \phi}, \quad M = \frac{8 \alpha_\infty \eta}{\sigma \phi \Lambda^2}, \quad (\text{B.1})$$

360 where $i = \sqrt{-1}$, η the viscosity, ϕ and α_∞ are respectively the porosity and tortuosity
 361 of the porous medium, Λ is the viscous characteristic length, $k_0 = \frac{\eta}{\sigma}$, is an intrinsic
 362 parameter depending on the geometry of the pores (σ , the flow resistivity).

363 The dynamic scaled compressibility is given by [22]

$$364 \quad \beta(\omega) = \gamma - (\gamma - 1) \times \left(1 + \frac{1}{i\varpi'} \sqrt{1 + \frac{M}{2} i\varpi'} \right)^{-1}, \quad \varpi' = \frac{\omega \rho_f k'_0 P_r}{\eta \phi}, \quad M' = \frac{8k'_0}{\phi \Lambda'^2}, \quad (\text{B.2})$$

364 where ϖ' is the reduced frequency, γ is the ratio of specific heats of the saturating gas,
 365 Λ' is the thermal characteristic length, P_r is the Prandtl number. The static thermal
 366 permeability k'_0 which partly characterizes the thermal effects at *low frequencies* (when
 367 the thermal boundary layer is of the same order of magnitude of the characteristic size
 368 of the pores).

369 **Appendix C. Expressions for the wavenumbers**

370 *The Helmholtz-Hodge decomposition*

371 In order to calculate the wavenumbers, the solid and fluid displacements are first
 372 decomposed into scalar (φ) and vector potential (ψ) components using the Helmholtz-
 373 Hodge decompositions:

$$\mathbf{u} = \nabla \varphi_s + \nabla \times \psi_s, \quad \mathbf{U} = \nabla \varphi_f + \nabla \times \psi_f. \quad (\text{C.1})$$

374 This can be extended to include the filtration \mathbf{w}

$$\mathbf{w} = \phi(\mathbf{u} - \mathbf{U}) = \nabla \varphi + \nabla \times \psi. \quad (\text{C.2})$$

375 Since the gradient and curl operators are linear, the following relations can be deduced
 376 $\varphi = \phi(\varphi_s - \varphi_f)$ and $\psi = \phi(\psi_s - \psi_f)$.

377 The expressions for the compressional wavenumbers and the rotational wavenum-
 378 ber are given in the following sections. The solutions to the equations provide three
 379 wavenumbers for the waves propagating in the solid (one compressional and one shear
 380 wave) and in the fluid (compressional wave).

381 *Volumetric/dilational ($\Theta = \nabla \cdot \mathbf{u} \neq 0$) or compressional wave wavenumber*

382 Using plane wave potentials, $\varphi_s = \Phi_j^s \exp(i(-\omega t + \mathbf{k}\mathbf{r}))$, $\varphi_f = \Phi_j^f \exp(i(-\omega t + \mathbf{k}\mathbf{r}))$
 383 for the curl-free motion ($\nabla \times \mathbf{u} = 0$) (the subscripts and subscripts s , f represent the
 384 solid and fluid) a matrix equation is derived

$$\begin{bmatrix} -(C\phi + H)k^2 + (\rho_f\phi + \rho)\omega^2 & \phi(Ck^2 - \omega^2\rho_f) \\ -(M\phi + C)k^2 + (\tilde{\varrho}(\omega)\phi + \rho_f)\omega^2 & \phi(Mk^2 - \omega^2\tilde{\varrho}(\omega)) \end{bmatrix} \begin{bmatrix} \varphi_s \\ \varphi_f \end{bmatrix} = \begin{bmatrix} 0 \\ 0 \end{bmatrix}, \quad (\text{C.3})$$

385 where $k^2 = \mathbf{k} \cdot \mathbf{k}$ with \mathbf{k} the complex wavenumber, $\tilde{\varrho}(\omega) = \frac{\rho_f}{\phi} \tilde{\alpha}(\omega)$.

386 The solution to this matrix equation provides two wavenumbers for the waves propa-
387 gating in the saturated poroelastic medium, one solid borne and the second fluid borne.

$$k_{1,2}^2 = \omega^2 \left\{ \frac{-(\tilde{\varrho}(\omega)H + \rho M - 2\rho_f C) \pm \sqrt{\Delta}}{2(C^2 - HM)} \right\}, \quad (\text{C.4})$$

388 where $\Delta = (\tilde{\varrho}(\omega)H - \rho M)^2 + 4(\rho_f H - \tilde{\varrho}(\omega)C)(\rho_f M - \tilde{\varrho}(\omega)C)$

389 *The rotational or shear wave wavenumber*

390 The equivoluminal, rotational ($\Theta = \nabla \cdot \mathbf{u} = 0$) wavenumber is derived using plane
391 wave potentials, $\psi_s = \Phi_3^s \exp(i(-\omega t + \mathbf{k}\mathbf{r}))$, $\psi_f = \Phi_3^f \exp(i(-\omega t + \mathbf{k}\mathbf{r}))$. The matrix
392 equation is given by

$$\begin{bmatrix} -\mu k^2 + (\phi\rho_f + \rho)\omega^2 & -\phi\rho_f\omega^2 \\ (\phi\tilde{\varrho}(\omega) + \rho_f)\omega^2 & -\phi\tilde{\varrho}(\omega)\omega^2 \end{bmatrix} \begin{bmatrix} \psi_s \\ \psi_f \end{bmatrix} = \begin{bmatrix} 0 \\ 0 \end{bmatrix}, \quad (\text{C.5})$$

393 From which the shear wavenumber is

$$k_3^2 = \frac{\rho\omega^2}{\mu} \left(1 - \frac{\rho_f^2}{\tilde{\varrho}(\omega)\rho} \right) \quad (\text{C.6})$$

394 *Appendix C.1. The relationships between the solid and fluid displacements*

395 The ratios between the displacement potentials of the fluid motion and solid in com-
396 pressional motion are given by:

$$\mu_{1,2} = \frac{\Phi_j^f}{\Phi_j^s} = \frac{k_j^2(C\phi + H) - \omega^2(\rho + \phi\rho_f)}{(Ck_j^2 - \omega^2\rho_f)\phi}, \quad j = 1, 2. \quad (\text{C.7})$$

397 The ratio between the displacements potentials of the fluid and solid in shear motion is
398 given by:

$$\mu_3 = \frac{\Phi_3^f}{\Phi_3^s} = 1 - \frac{k_3^2\mu}{\phi\rho_f\omega^2} + \frac{\rho}{\phi\rho_f}. \quad (\text{C.8})$$

399 **Appendix D. The transfer matrix formulation**

400 The incident and reflected plane wave potentials in the layer for ψ and φ are expressed
401 in the Laplace domain $(\mathfrak{L}[f(t)])(p) = \int_0^\infty f(t)e^{-pt} dt$ as:

$$\psi_j^s = (\Phi_j \exp(-\mathcal{K}_j^z z) + \Phi_j' \exp(\mathcal{K}_j^z z)) \exp(-\mathcal{K}_j^x x), \quad j = 1, 2 \quad (\text{D.1})$$

$$\varphi_3^s = (\Phi_3 \exp(-\mathcal{K}_3^z z) + \Phi_3' \exp(\mathcal{K}_3^z z)) \exp(-\mathcal{K}_3^x x), \quad (\text{D.2})$$

$$\psi_j^f = \mu_j \psi_j^s, \quad j = 1, 2, \quad \varphi_3^f = \mu_3 \varphi_3^s, \quad (\text{D.3})$$

402 where Φ_m et Φ_m' , ($m = 1, 2, 3$) are the amplitudes of the incident and reflected waves,
403 respectively, $\mathcal{K}_j^z = i\chi_j$ et $\mathcal{K}_j^x = i\gamma_j$ where

$$\begin{aligned} \gamma_f &= k_f \sin(\theta), \quad \mathcal{K}_f = i\sqrt{k_f^2 - \gamma_f^2}, \\ \gamma_j &= k_j \sin(\theta), \quad j = 1, 2, 3 \\ \chi_j &= \sqrt{k_j^2 - \gamma_j^2}, \quad j = 1, 2, 3. \end{aligned} \quad (\text{D.4})$$

404 The vector \mathbf{A} is then obtained through expansion of the potentials in Eq. D.1 (see
405 also [34] for the purely elastic case), for example:

$$\bar{\Phi}_1 e^{-\kappa_1^z z} + \bar{\Phi}_1' e^{\kappa_1^z z} = (\bar{\Phi}_1 + \bar{\Phi}_1') \cosh(\kappa_1^z z) - (\bar{\Phi}_1 - \bar{\Phi}_1') \sinh(\kappa_1^z z). \quad (\text{D.5})$$

406 After substitution, the vector takes the form:

$$\mathbf{A} = \left[\begin{array}{cccccc} \bar{\Phi}_1 + \bar{\Phi}_1' & \bar{\Phi}_1 - \bar{\Phi}_1' & \bar{\Phi}_2 + \bar{\Phi}_2' & \bar{\Phi}_2 - \bar{\Phi}_2' & \bar{\Phi}_3 + \bar{\Phi}_3' & \bar{\Phi}_3 - \bar{\Phi}_3' \end{array} \right]^T.$$

407 The characteristic transfer matrix propagation equations in Eq. (6) can be simplified:

$$\mathbf{V}(M_{\Gamma_m^+}) = [\mathbf{T}]\mathbf{V}(M_{\Gamma_{m+1}^-}), \quad (\text{D.6})$$

408 where the transfer matrix $[\mathbf{T}] = [\mathbf{T}_m(-d1)][\mathbf{T}_m(0)]^{-1}$. The matrix $[\mathbf{T}_m(z)]$ is given
409 in Appendix E.

410 In this study, we present results for a bilayer composed of two air saturated poroelastic
411 materials.

412 *The boundary conditions between two poroelastic layers*

413 The second poroelastic layer is placed after the first one so that the points at the
 414 Γ_2^+ are inside the second layer (Fig. 1). Thus, the boundary conditions for the coupling
 415 between two poroelastic layers are:

- 416 • continuity of the solid velocity vector,
- 417 • conservation of the fluid flow,
- 418 • continuity of the normal and tangential components of the total stress traction
 419 acting on the interface,
- 420 • continuity of the pressure in the fluid phase.

421 The equations of the conditions of continuity between two poroelastic layers are therefore:

$$\dot{u}_x^s(M_{\Gamma_m^-}) = \dot{u}_x^s(M_{\Gamma_m^+}), \quad (\text{D.7})$$

$$\dot{u}_z^s(M_{\Gamma_m^-}) = \dot{u}_z^s(M_{\Gamma_m^+}), \quad (\text{D.8})$$

$$\phi_{m-1} \left(\dot{u}_z^f(M_{\Gamma_m^-}) - \dot{u}_z^s(M_{\Gamma_m^-}) \right) = \phi_m \left(\dot{u}_z^f(M_{\Gamma_m^+}) - \dot{u}_z^s(M_{\Gamma_m^+}) \right), \quad (\text{D.9})$$

$$\tau_{zz}^s(M_{\Gamma_m^-}) + \tau_{zz}^f(M_{\Gamma_m^-}) = \tau_{zz}^s(M_{\Gamma_m^+}) + \tau_{zz}^f(M_{\Gamma_m^+}), \quad (\text{D.10})$$

$$\tau_{xz}^s(M_{\Gamma_m^-}) = \tau_{xz}^s(M_{\Gamma_m^+}), \quad (\text{D.11})$$

$$\frac{\tau_{zz}^f(M_{\Gamma_m^-})}{\phi_{m-1}} = \frac{\tau_{zz}^f(M_{\Gamma_m^+})}{\phi_m}, \quad (\text{D.12})$$

422 where ϕ_{m-1} and ϕ_m are the porosities of the first and second poroelastic layers ($m = 2$).

423 This results in a coupling matrix (C^M) that provides interface for the two poroelastic
 424 layers, m and $m - 1$:

$$C_{12}^M = \begin{bmatrix} 1 & 0 & 0 & 0 & 0 & 0 \\ 0 & 1 & 0 & 0 & 0 & 0 \\ 0 & 1 - \frac{\phi_m}{\phi_{m-1}} & \frac{\phi_m}{\phi_{m-1}} & 0 & 0 & 0 \\ 0 & 0 & 0 & 1 & 0 & 1 - \frac{\phi_{m-1}}{\phi_m} \\ 0 & 0 & 0 & 0 & 1 & 0 \\ 0 & 0 & 0 & 0 & 0 & \frac{\phi_{m-1}}{\phi_m} \end{bmatrix} \quad (\text{D.13})$$

425 The global matrix for the two layers can be written as:

$$\mathbf{T}^g = [\mathbf{T}_1][C_{12}^M][\mathbf{T}_2], \quad (\text{D.14})$$

426 where $[\mathbf{T}_1]$ and $[\mathbf{T}_2]$ are the transfer matrices of the first and second poroelastic layers.

427 *The m stratified layers are bounded on both sides by fluids of semi-infinite extent touching*
 428 Γ_1 and Γ_{m+1}

429 When the stratified porous medium is open to a semi-infinite fluid medium on Γ_{m+1}
 430 (Fig. 3), the conditions of continuity are:

$$\begin{aligned}
 (1 - \phi_m)v_z^s(M_{\Gamma_{m+1}^-}) + \phi_m v_z^f(M_{\Gamma_{m+1}^-}) &= v_z^f(M_{\Gamma_{m+1}^+}), \\
 \tau_{zz}^s(M_{\Gamma_{m+1}^-}) &= -(1 - \phi_m)p(M_{\Gamma_{m+1}^+}), \\
 \tau_{xz}^s(M_{\Gamma_{m+1}^-}) &= 0, \\
 \tau_{zz}^f(M_{\Gamma_{m+1}^-}) &= -\phi_m p(M_{\Gamma_{m+1}^+}), \tag{D.15}
 \end{aligned}$$

431 where $p(M_{\Gamma_{m+1}^+})$ and $\dot{u}_z^f(M_{\Gamma_{m+1}^+})$ are the acoustic pressure and velocity at a point on
 432 $\mathbf{V}^f(M_{\Gamma_{m+1}^+}) = [p(M_{\Gamma_{m+1}^+}) \quad \dot{u}_z^f(M_{\Gamma_{m+1}^+})]^T$ in the fluid, and $Z_{\Gamma_{m+1}^+}$ is the acoustic impedance.

433 By introducing the transmission coefficient ($p(M_{\Gamma_{m+1}^+}) = T p_i \cos(\theta)$), the condition
 434 in Eq. (D.15) can be written in matrix form:

$$\begin{aligned}
 \mathbf{I}_f^m \mathbf{V}^m(M_{\Gamma_{m+1}^-}) &= \begin{bmatrix} 0 & 1 - \phi_m & \phi_m & 0 & 0 & 0 \\ 0 & 0 & 0 & 1 & 0 & 0 \\ 0 & 0 & 0 & 0 & 1 & 0 \\ 0 & 0 & 0 & 0 & 0 & 1 \end{bmatrix} \times \begin{bmatrix} \dot{u}_x^s(M_{\Gamma_{m+1}^-}) \\ \dot{u}_z^s(M_{\Gamma_{m+1}^-}) \\ \dot{u}_z^f(M_{\Gamma_{m+1}^-}) \\ \tau_{zz}^s(M_{\Gamma_{m+1}^-}) \\ \tau_{xz}^s(M_{\Gamma_{m+1}^+}) \\ \tau_{zz}^f(M_{\Gamma_{m+1}^-}) \end{bmatrix} = \begin{bmatrix} 0 & 1 \\ -(1 - \phi_m) & 0 \\ 0 & 0 \\ -\phi_m & 0 \end{bmatrix} \times \\
 \left[p(M_{\Gamma_{m+1}^+}) \dot{u}_z^f(M_{\Gamma_{m+1}^+}) \right] &= \mathbf{J}_f^m \mathbf{V}^f(M_{\Gamma_{m+1}^+}) = \begin{bmatrix} T/Z(M_{\Gamma_{m+1}^+}) \\ -(1 - \phi_m)T \\ 0 \\ -\phi_m T \end{bmatrix} p_i \cos(\theta) \tag{D.16}
 \end{aligned}$$

435 On the left hand side of the stratified layer (Fig. 1), the continuity conditions at

436 points lying in the fluid at the interface Γ_1^- of the first layer are given by:

$$\begin{aligned}
(1 - \phi_1)\dot{u}_z^s(M_{\Gamma_1^+}) + \phi_1\dot{u}_z^f(M_{\Gamma_1^+}) &= v(M_{\Gamma_1^-}), \\
\tau_{zz}^s(M_{\Gamma_1^+}) &= -(1 - \phi_1)p(M_{\Gamma_1^-}), \\
\tau_{xz}^s(M_{\Gamma_1^+}) &= 0, \\
\tau_{zz}^f(M_{\Gamma_1^+}) &= -\phi_1p(M_{\Gamma_1^-}), \tag{D.17}
\end{aligned}$$

437 where $v(M_{\Gamma_1^-}) = (1 - R)p(M_{\Gamma_1^-})/Z(M_{\Gamma_1^-})$ and $p(M_{\Gamma_1^-}) = p_i \cos(\theta)$ is the velocity of
438 the particles at point $M_{\Gamma_1^-}$ in the fluid, and $Z(M_{\Gamma_1^-})$ is the acoustic impedance. These
439 conditions can finally be written in matrix form:

$$\mathbf{I}_f^1 \mathbf{V}^1(M_{\Gamma_1^-}) = \begin{bmatrix} 0 & 1 \\ -(1 - \phi_1) & 0 \\ 0 & 0 \\ -\phi_1 & 0 \end{bmatrix} \begin{bmatrix} p(M_{\Gamma_1^-}) \\ \dot{u}_z^f(M_{\Gamma_1^-}) \end{bmatrix} = \mathbf{J}_f^1 \mathbf{V}^f(M_{\Gamma_1^-}) = \begin{bmatrix} (1 - R)/Z(M_{\Gamma_1^-}) \\ -(1 - \phi_1)(1 + R) \\ 0 \\ -\phi_1(1 + R) \end{bmatrix} p_i \cos(\theta), \tag{D.18}$$

440 where

$$\mathbf{J}_f^1 = \begin{bmatrix} 0 & 1 - \phi_1 & \phi_1 & 0 & 0 & 0 \\ 0 & 0 & 0 & 1 & 0 & 0 \\ 0 & 0 & 0 & 0 & 1 & 0 \\ 0 & 0 & 0 & 0 & 0 & 1 \end{bmatrix}. \tag{D.19}$$

441 Using the previous relationships given in Eqns.(D.16) and (D.18), the transfer matrix
442 equation is then derived and given in Eq. (D.20):

$$\begin{aligned}
\mathbf{I}_f^1 \mathbf{T}^g \mathbf{V}(M_{\Gamma_{m+1}^-}) &= \begin{bmatrix} 0 & 1 - \phi_1 & \phi_1 & 0 & 0 & 0 \\ 0 & 0 & 0 & 1 & 0 & 0 \\ 0 & 0 & 0 & 0 & 1 & 0 \\ 0 & 0 & 0 & 0 & 0 & 1 \end{bmatrix} \times \begin{bmatrix} T_{11}^g & T_{12}^g & T_{13}^g & T_{14}^g & T_{15}^g & T_{16}^g \\ T_{21}^g & T_{22}^g & T_{23}^g & T_{24}^g & T_{25}^g & T_{26}^g \\ T_{31}^g & T_{32}^g & T_{33}^g & T_{34}^g & T_{35}^g & T_{36}^g \\ T_{41}^g & T_{42}^g & T_{43}^g & T_{44}^g & T_{45}^g & T_{46}^g \\ T_{51}^g & T_{52}^g & T_{53}^g & T_{54}^g & T_{55}^g & T_{56}^g \\ T_{61}^g & T_{62}^g & T_{63}^g & T_{64}^g & T_{55}^g & T_{66}^g \end{bmatrix} \times \\
&\begin{bmatrix} \dot{u}_x^s(M_{\Gamma_{m+1}^+}) \\ \dot{u}_z^s(M_{\Gamma_{m+1}^+}) \\ \dot{u}_z^f(M_{\Gamma_{m+1}^+}) \\ \tau_{zz}^s(M_{\Gamma_{m+1}^+}) \\ \tau_{xz}^s(M_{\Gamma_{m+1}^+}) \\ \tau_{zz}^f(M_{\Gamma_{m+1}^+}) \end{bmatrix} = \mathbf{J}_f^1 \mathbf{V}^f(M_{\Gamma_1^-}). \tag{D.20}
\end{aligned}$$

443 Appendix E. Derivation of the transfer matrix members

444 The total wave potential for the compressional waves is:

$$\psi_t^s = \psi_1^s + \psi_2^s, \quad \psi_t^f = \psi_1^f + \psi_2^f. \tag{E.1}$$

445 The stress-strain relations are obtained from the strain energy W such that $\tau_{ij} =$

$$446 \frac{1}{2} \left(\frac{\partial W}{\partial \varepsilon_{ij}} + \frac{\partial W}{\partial \varepsilon_{ji}} \right)$$

$$\begin{aligned}
\tau_{xx} &= \frac{\partial W}{\partial \varepsilon_x} = 2\mu\varepsilon_x + \lambda_c\varepsilon - \alpha_B M\xi, \\
\tau_{zz} &= \frac{\partial W}{\partial \varepsilon_z} = 2\mu\varepsilon_z + \lambda_c\varepsilon - \alpha_B M\xi, \\
\tau_{zx} &= \frac{\partial E}{\partial \gamma_y} = \mu\gamma_y, \\
p_f &= \frac{\partial E}{\partial \xi} = M\xi - C\varepsilon, \tag{E.2}
\end{aligned}$$

447 where $\varepsilon = \varepsilon_x + \varepsilon_y + \varepsilon_z$, $\varepsilon_x = \frac{\partial u_x}{\partial x}$, $\varepsilon_z = \frac{\partial u_z}{\partial z}$, $\gamma_y = \frac{\partial u_z}{\partial x} + \frac{\partial u_x}{\partial z}$ and $\xi = \frac{\partial u_z}{\partial x} + \frac{\partial u_x}{\partial z}$.

448 The components of the displacements are derived from the Helmholtz-Hodge decom-
 449 position (Eq. (C.1))

$$u_x^s = \frac{\partial}{\partial x} \psi_t^s - \frac{\partial}{\partial z} \varphi_3^s, \quad u_z^s = \frac{\partial}{\partial z} \psi_t^s + \frac{\partial}{\partial x} \varphi_3^s, \quad (\text{E.3})$$

450 from which the wave velocities are derived:

$$\begin{aligned} \tilde{v}_x^s &= p \left(\frac{\partial}{\partial x} \psi_t^s - \frac{\partial}{\partial z} \varphi_3^s \right), \quad \tilde{v}_z^s = p \left(\frac{\partial}{\partial z} \psi_t^s + \frac{\partial}{\partial x} \varphi_3^s \right), \\ \tilde{v}_z^f &= p \left(\mu_1 \frac{\partial}{\partial z} \psi_1^s + \mu_2 \frac{\partial}{\partial z} \psi_2^s \right) + p \mu_3 \frac{\partial}{\partial z} \varphi_3^s. \end{aligned} \quad (\text{E.4})$$

451 Using the above relations provides the matrix of the stresses and velocities in the fluid
 452 saturated poroelastic layer.

453

$$\mathbf{T}_m(z) = \begin{bmatrix} -p \cosh(\kappa z_1 z) \kappa_f & p \sinh(\kappa z_1 z) \kappa_f & -p \cosh(\kappa z_2 z) \kappa_f & p \sinh(\kappa z_2 z) \kappa_f & -p \sinh(\kappa z_3 z) \kappa_{z_3} & p \cosh(\kappa z_3 z) \kappa_{z_3} \\ p \sinh(\kappa z_1 z) \kappa_{z_1} & -p \kappa_{z_1} \cosh(\kappa z_1 z) & p \sinh(\kappa z_2 z) \kappa_{z_2} & -p \kappa_{z_2} \cosh(\kappa z_2 z) & -p \cosh(\kappa z_3 z) \kappa_f & p \sinh(\kappa z_3 z) \kappa_f \\ p \sinh(\kappa z_1 z) \mu_1 \kappa_{z_1} & -p \cosh(\kappa z_1 z) \mu_1 \kappa_{z_1} & p \sinh(\kappa z_2 z) \mu_2 \kappa_{z_2} & -p \cosh(\kappa z_2 z) \mu_2 \kappa_{z_2} & -p \cosh(\kappa z_3 z) \mu_3 \kappa_f & p \sinh(\kappa z_3 z) \mu_3 \kappa_f \\ s_1 \cosh(\kappa z_1 z) & -s_1 \sinh(\kappa z_1 z) & s_2 \cosh(\kappa z_2 z) & -s_2 \sinh(\kappa z_2 z) & -2 \mu_3 \kappa_f \kappa_{z_3} \mu \sinh(\kappa z_3 z) & 2 \cosh(\kappa z_3 z) \mu \mu_3 \kappa_f \kappa_{z_3} \\ -2 \mu \sinh(\kappa z_1 z) \kappa_f \kappa_{z_1} & 2 \mu \kappa_f \cosh(\kappa z_1 z) \kappa_{z_1} & -2 \mu \kappa_f \sinh(\kappa z_2 z) \kappa_{z_2} & 2 \mu \cosh(\kappa z_2 z) \kappa_f \kappa_{z_2} & \mu (\kappa_f^2 - \kappa_{z_3}^2) \cosh(\kappa z_3 z) & \mu (\kappa_{z_3}^2 - \kappa_f^2) \sinh(\kappa z_3 z) \\ s_3 \cosh(\kappa z_1 z) & -s_3 \sinh(\kappa z_1 z) & s_4 \cosh(\kappa z_2 z) & -s_4 \sinh(\kappa z_2 z) (\kappa_f^2 + \kappa_{z_2}^2) & 0 & 0 \end{bmatrix}, \quad (\text{E.5})$$

where,

$$\begin{aligned}
s_1 &= (M\phi (\kappa_f^2 + \kappa_{z_1}^2) (\mu_1 - 1) \alpha_B + \kappa_f^2 \lambda_c + \kappa_{z_1}^2 (\lambda_c + 2\mu)), \\
s_2 &= (M\phi (\kappa_f^2 + \kappa_{z_2}^2) (\mu_2 - 1) \alpha_B + \kappa_f^2 \lambda_c + \kappa_{z_2}^2 (\lambda_c + 2\mu)), \\
s_3 &= M\phi (\kappa_f^2 + \kappa_{z_1}^2) ((\mu_1 - 1) \phi + \alpha_B), \\
s_4 &= M\phi ((\mu_2 - 1) \phi + \alpha_B) (\kappa_f^2 + \kappa_{z_2}^2).
\end{aligned}$$

455 References

- 456 [1] R. F. Gibson. *Principles of Composite Material Mechanics*. McGraw-Hill, New York, 1989.
- 457 [2] Erick Ogam, Z.E.A. Fella, and Géry Ogam. Identification of the mechanical moduli of closed-cell
458 porous foams using transmitted acoustic waves in air and the transfer matrix method. *Composite*
459 *Structures*, 135:205 – 216, 2016.
- 460 [3] N. Sebaa, Z. E. A. Fella, M. Fella, W. Lauriks, and C. Depollier. Measuring flow resistivity of
461 porous material via acoustic reflected waves. *J. Appl. Phys.*, 98(8):084901, 2005.
- 462 [4] Z. E. A Fella, M. Fella, F. G. Mitri, N. Sebaa, C. Depollier, , and W. Lauriks. Measuring
463 permeability of porous materials at low frequency range via acoustic transmitted waves. *Review of*
464 *Scientific Instruments*, 78(11):–, 2007.
- 465 [5] M. Sadouki, Z. E. A. Fella, A. Berbiche, M. Fella, F. G. Mitri, E. Ogam, and C. Depollier. Mea-
466 suring static viscous permeability of porous absorbing materials. *J. Acoust. Soc. Am.*, 135(6):3163–
467 3171, 2014.
- 468 [6] R. Roncen, Z. E. A. Fella, D. Lafarge, E. Piot, F. Simon, E. Ogam, M. Fella, and C. Depollier.
469 Acoustical modeling and bayesian inference for rigid porous media in the low-mid frequency regime.
470 *J. Acoust. Soc. Am.*, 144(6):3084–3101, 2018.
- 471 [7] A. N. Norris. On the viscodynamic operator in Biot’s equations of poroelasticity. *J. Wave-Material*
472 *Interaction*, 1(4):365–380, 1986.
- 473 [8] R. Roncen, Z. E. A. Fella, E. Piot, F. Simon, E. Ogam, M. Fella, and C. Depollier. Inverse
474 identification of a higher order viscous parameter of rigid porous media in the high frequency
475 domain. *J. Acoust. Soc. Am.*, 145(3):1629–1639, 2019.
- 476 [9] J. Y. Chung and D. A. Blaser. Transfer function method of measuring in-duct acoustic properties.
477 i. theory. *J. Acoust. Soc. Am.*, 68(3):907–913, 1980.
- 478 [10] Mohamed Ben Mansour, Erick Ogam, Ahmed Jelidi, Amel Soukaina Cherif, and Sadok Ben Jabral-
479 lah. Influence of compaction pressure on the mechanical and acoustic properties of compacted earth
480 blocks: An inverse multi-parameter acoustic problem. *Appl. Acoust.*, 125:128–135, 2017.
- 481 [11] Ulhas Arun Malawade and M.G. Jadhav. Investigation of the acoustic performance of bagasse. *J.*
482 *Mater. Res. Technol.*, 9(1):882–889, 2020.
- 483 [12] O. Doutres, Y. Salissou, N. Atalla, and R. Panneton. Evaluation of the acoustic and non-acoustic
484 properties of sound absorbing materials using a three-microphone impedance tube. *Appl. Acoust.*,
485 71(6):506 – 509, 2010.
- 486 [13] L. E. Kinsler, , A. R. Frey, A. B. Coppens, and J. V. Sanders. *Fundamentals of Acoustics*. Wiley,
487 New Jersey, USA, fourth edition, 2000.
- 488 [14] P. M. Morse and K. U. Ingard. *Theoretical acoustics*. McGraw-Hill, Inc, New York, 1968.
- 489 [15] Erick Ogam and Z. E. A. Fella. Recovery of biot’s transition frequency of air-saturated poroelastic
490 media using vibroacoustic spectroscopy. *J. Appl. Phys.*, 116(6):063503, 2014.
- 491 [16] Erick Ogam, Z. E. A Fella, and Paul Baki. The inverse problem of acoustic wave scattering by an
492 air-saturated poroelastic cylinder. *J. Acoust. Soc. Am.*, 133(3):1443–1457, 2013.

- 493 [17] M. A. Biot. Generalized theory of acoustic propagation in porous dissipative media. *J. Acoust. Soc.*
494 *Am.*, 34(5):1254–1264, 1962.
- 495 [18] J.-F Allard and N. Atalla. *Propagation of Sound in Porous Media: Modelling Sound Absorbing*
496 *Materials*. John Wiley and Sons, 2nd edition, 2009.
- 497 [19] James G. Berryman. Origin of Gassmann’s equations. *Geophysics*, 64(5):1627–1629, 1999.
- 498 [20] D. L. Johnson, J. Koplik, and R. Dashen. Theory of dynamic permeability and tortuosity in fluid-
499 saturated porous media. *J. fluid mech.*, 176(1):379–402, 1987.
- 500 [21] Y. Champoux and J. F. Allard. Dynamic tortuosity and bulk modulus in air-saturated porous
501 media. *J. Appl. Phys.*, 70:1975–1979, 1991.
- 502 [22] D. Lafarge, P. Lemarinier, J.-F. Allard, and V. Tarnow. Dynamic compressibility of air in porous
503 structures at audible frequencies. *J. Acoust. Soc. Am.*, 102(4):1995–2006, 1997.
- 504 [23] Jeff Bezanson, Alan Edelman, Stefan Karpinski, and Viral B Shah. Julia: A fresh approach to
505 numerical computing. *SIAM review*, 59(1):65–98, 2017.
- 506 [24] M. A. Biot. Mechanics of deformation and acoustic propagation in porous media. *J. Appl. Phys.*,
507 33(4):1482–1498, 1962.
- 508 [25] Y. Champoux and Michael R. Stinson. On acoustical models for sound propagation in rigid frame
509 porous materials and the influence of shape factors. *J. Acoust. Soc. Am.*, 92(2):1120–1131, 1992.
- 510 [26] Maurice A. Biot and D. G. Willis. The elastic coefficients of the theory of consolidation. *J. Appl.*
511 *Mech.*, 24:594–601, 1957.
- 512 [27] Lorna J. Gibson and Michael F. Ashby. *Cellular Solids: Structure and Properties*. Cambridge Solid
513 State Science Series. Cambridge University Press, 1999.
- 514 [28] J.-P. Groby, E. Ogam, L. De Ryck, N. Sebaa, and W. Lauriks. Analytical method for the ultrasonic
515 characterization of homogeneous rigid porous materials from transmitted and reflected coefficients.
516 *J. Acoust. Soc. Am.*, 127(2):764–772, 2010.
- 517 [29] E. Ogam, Z.E.A. Fellah, N. Sebaa, and J.-P Groby. Non-ambiguous recovery of Biot poroelastic
518 parameters of cellular panels using ultrasonic waves. *J. Sound Vib.*, 330(6):1074 – 1090, 2011.
- 519 [30] Bryan H. Song and J. Stuart Bolton. Investigation of the vibrational modes of edge-constrained
520 fibrous samples placed in a standing wave tube. *J. Acoust. Soc. Am.*, 113(4):1833–1849, 2003.
- 521 [31] Thomas Dupont, Philippe Leclaire, Raymond Panneton, Kévin Verdière, and Saïd Elkoun. A
522 method for measuring the acoustic properties of a porous sample mounted in a rigid ring in acoustic
523 tubes. *J. Acoust. Soc. Am.*, 133(5):3242–3242, 2013.
- 524 [32] Lawrence R. Rabiner and Bernard Gold. *Theory and Application of Digital Signal Processing*. NJ:
525 Prentice-Hall, Englewood Cliffs, 1975.
- 526 [33] Steven M Kay. *Modern Spectral Estimation*. NJ: Prentice-Hall, Englewood Cliffs, 1988.
- 527 [34] L. M. Brekhovskikh. *Waves in layered Media*. Academic Press, New York, NY, USA, 1960.